

# Eagle-Eye Inspired Meta-Device for Phase Imaging

Junxiao Zhou, Fanglin Tian, Jie Hu, Zhixia(Linda) Shi, Veronica Gomez Godinez, Din Ping Tsai,\* and Zhaowei Liu\*

The dual-focus vision observed in eagles' eyes is an intriguing phenomenon captivates scientists since a long time. Inspired by this natural occurrence, the authors' research introduces a novel bifocal meta-device incorporating a polarized camera capable of simultaneously capturing images for two different polarizations with slightly different focal distances. This innovative approach facilitates the concurrent acquisition of underfocused and overfocused images in a single snapshot, enabling the effective extraction of quantitative phase information from the object using the transport of intensity equation. Experimental demonstrations showcase the application of quantitative phase imaging to artificial objects and human embryonic kidney cells, particularly emphasizing the meta-device's relevance in dynamic scenarios such as laser-induced ablation in human embryonic kidney cells. Moreover, it provides a solution for the quantification during the dynamic process at the cellular level. Notably, the proposed eagle-eye inspired meta-device for phase imaging (EIMPI), due to its simplicity and compact nature, holds promise for significant applications in fields such as endoscopy and headsets, where a lightweight and compact setup is essential.

structure of shark skin contribute to the design of waterborne vehicles with reduced water resistance. The micro-nanostructures on lotus plant leaves, known as the lotus effect, have inspired the application of self-cleaning surface designs in construction materials and coatings.<sup>[1]</sup> The eyes of eagles are equally remarkable, featuring two convex lenses for both nearsightedness and farsightedness. This distinctive ocular structure enables eagles to perceive objects at varying distances with clarity, obviating the need, as in the case of humans, to adjust the focal length of their eyes. Imaging biological cells and tissues is crucial for advancing biological research and medical diagnostics. Non-invasive methodologies, such as phase contrast and differential interference contrast methods, particularly exhibit favorable compatibility with biological samples.<sup>[2,3]</sup> Recently, quantitative phase imaging (QPI) has gained popularity for its capacity to provide precise quantitative information,

establishing itself as a highly consequential technique.<sup>[4,5]</sup> Demonstrating its versatility, QPI technology has made significant contributions in medical contexts by exploring the biophysical and pathophysiological properties of red blood cells,<sup>[4]</sup> measuring single-cell volume and weight over time,<sup>[6]</sup> and quantifying cancer cell phenotypes.<sup>[7]</sup>

The existing techniques for QPI can be classified into interferometric and non-interferometric methods. Common path interferometry methods, such as shear interferometry, resolve the instability in QPI observed in interferometric methods, attributed to time-varying phase noise, by eliminating the requirement for a reference. Non-interferometric approaches encompass differential phase contrast,<sup>[8]</sup> Fourier ptychographic microscopy,<sup>[9]</sup> and transport intensity equations (TIE).<sup>[10]</sup> among others.<sup>[11]</sup> In contrast to the former, which requires modulating the illumination, TIE can be considered as modulating the detection, capturing intensity images at different defocused planes. This approach proves its effectiveness in incoherent light and provides a direct unwrapped phase value. Recent advancements in nano-photonics have opened possibilities for exploring ingeniously designed nanostructured planar elements. A meta-device, utilizing artificially designed structures with subwavelength sizes,<sup>[12,13]</sup> can effectively manipulate electromagnetic fields in smaller dimensions, offering novel optical functionalities.<sup>[14–23]</sup> and achieving QPI through existing techniques.<sup>[24–28]</sup> It does so, especially, by employing ingeniously

## 1. Introduction

In the natural world that sustains our existence, numerous animals and plants not only surpass humans in lifespan but also in independence. Consequently, when confronted with engineering challenges, humans frequently seek guidance and inspiration from the natural world. The invention of aircraft is largely attributed to the study of birds' wings; while, the unique texture and

J. Zhou, F. Tian, J. Hu, Z. Liu  
 Department of Electrical and Computer Engineering  
 University of California, San Diego  
 9500 Gilman Drive, La Jolla, CA 92093, USA  
 E-mail: [zhaowei@ucsd.edu](mailto:zhaowei@ucsd.edu)

J. Zhou, D. P. Tsai  
 Department of Electrical Engineering  
 City University of Hong Kong  
 Kowloon, Hong Kong 999077, China  
 E-mail: [dptsai@cityu.edu.hk](mailto:dptsai@cityu.edu.hk)

Z. Shi, V. G. Godinez  
 Institute of Engineering in Medicine  
 University of California, San Diego  
 La Jolla, San Diego, CA 92093, USA

 The ORCID identification number(s) for the author(s) of this article can be found under <https://doi.org/10.1002/adma.202402751>

DOI: 10.1002/adma.202402751

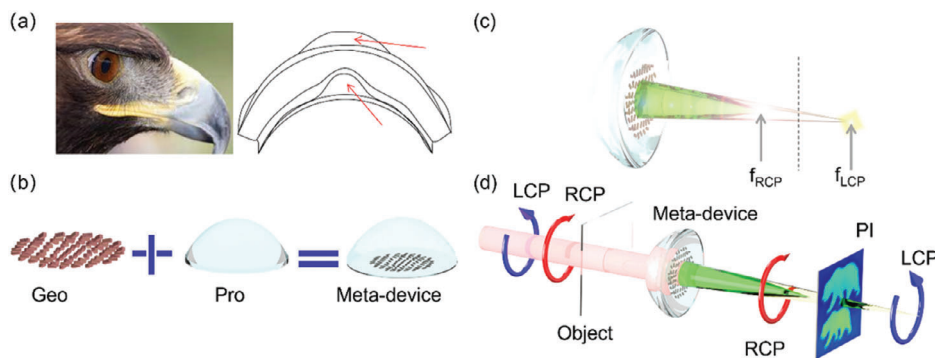


**Figure 1.** The concept figure of this work. a) Conceptual sketch of eagle eyes and its schematic representation. Reproduced with permission<sup>[32]</sup> Copyright 2023, BirdNote. b) The meta-device comprises the geometric phase lens and propagation phase lens. The right panel, a schematic figure, illustrates that the eagle's eye contains two foveae: a central fovea and a lateral fovea, located in separate regions of the eye, analogous to our PB phase lens and propagation phase. c,d) When linearly polarized (LP) light illuminates the meta-device, it spatially separates the LP light into left circularly polarized (LCP) and right circularly polarized (RCP) components at distinct locations along the propagation direction. A polarized camera, strategically positioned at the center between the two imaging planes, captures simultaneous underfocused and overfocused images. This concurrent acquisition facilitates the calculation of intensity differences between the captured images. Subsequently, this process enables the acquisition of QPI based on the TIE. PI is phase imaging.

designed metasurfaces for polarization-dependent components with two distinct focal points, within a  $4f$  optical system, positioning the metasurface on the Fourier plane of the object, and leveraging the transport of intensity equation (TIE) algorithm, the phase of the object can be reconstructed.<sup>[26,29]</sup> Increased design freedom can render the entire system with less components, smaller form factor, and higher optical efficiency. For example, employing the metasurface located at the Fourier plane or a pair of metasurface or two-layered metasurface design enables QPI. However, these require an expanded Fourier plane module, additional imaging lenses, or multiple measurements or can only obtain the phase gradient information instead of phase information. In addition, challenges arise from source coherence, system complexity, and compatibility with existing microscopy methods for user-friendly applications.

Here, drawing inspiration from the effective structure of the dual convex lenses found in the eagle eye, we propose the design of a meta-device that incorporates a polarized camera to achieve QPI for bioimaging applications. The initial component of our design comprises a meticulously arranged nano-structured array grounded in geometric phase principles. The subsequent component takes the form of a traditional convex lens calibrated to achieve the prescribed focal distance. The integration of the first two parts facilitates the establishment of dual focal planes at disparate positions, catering to distinct spins represented by left and right circular polarization (LCP and RCP). Such QPI capability is demonstrated by using a single meta-device in free space without any additional optical components. When the meta-device is combined with a bright-field microscope, phase imaging of human embryonic kidney (HEK) cells can be acquired with the diffraction limited resolution. Moreover, we extend our method to study dynamic processes such as laser ablation on cells, paving the way for laser surgery for tumors.

## 2. Results

**Figure 1** illustrates the schematic diagram of the bioinspired dual focus meta-device. The meta-device comprises a geometric phase

( $\Phi_{\text{Geo}}$ ) component and a propagation phase ( $\Phi_{\text{Pro}}$ ) component. The geometric phase component, including half-wave plate elements ( $|\phi_x - \phi_y| = \pi$ ) with spatially varying angular orientations  $\theta(x, y)$ , imposes a phase profile on a specific circular polarization [ $\Phi_{\text{Geo}}(x, y) = 2\theta(x, y)$ ]. These retarders effectuate the conversion of LCP (RCP) polarization to RCP (LCP) polarization, following a state-space trajectory dictated by the orientation of each element. Consequently, a geometric phase emerges, exhibiting a linear increase from 0 to  $2\pi$  as the element undergoes rotation within an angular range from 0 to  $\pi$ .<sup>[30,31]</sup> It is imperative to highlight that the phase profile imposed on LCP light is  $\Phi_{\text{Geo\_LCP}}(x, y)$ ; while, the phase profile conferred upon an RCP wavefront is inherently  $\Phi_{\text{Geo\_RCP}}(x, y) = -\Phi_{\text{Geo\_LCP}}(x, y)$  in an automatic manner. The Jones matrix of metasurface with a phase shift  $\pi$  and spatially varying local optical axes  $\theta$  is given by:  $T_{\text{MS}} = \begin{bmatrix} \cos 2\theta & \sin 2\theta \\ \sin 2\theta & -\cos 2\theta \end{bmatrix}$ . When an  $x$ -polarized incidence passes through the metasurface:

$$\begin{bmatrix} \cos 2\theta & \sin 2\theta \\ \sin 2\theta & -\cos 2\theta \end{bmatrix} \begin{bmatrix} 1 \\ 0 \end{bmatrix} = \frac{1}{2} \exp(-j2\theta) \begin{bmatrix} 1 \\ j \end{bmatrix} + \frac{1}{2} \exp(j2\theta) \begin{bmatrix} 1 \\ -j \end{bmatrix} \quad (1)$$

For the PB phase meta-device part, split the LCP and RCP components, where  $\theta(x, y) = \frac{2\pi}{\lambda} \left( \frac{x^2 + y^2}{4f_{\text{Geo}}} \right)$ .

As depicted in Figure 1b, to achieve the desired dual focus effect, the phase profile of the meta-device is described by the following expression (See Section S3, Supporting Information for more details):

$$\Phi_{(R,L)} = \Phi_{\text{Geo}} + \Phi_{\text{Pro}} \approx \sigma_{R,L} k \frac{x^2 + y^2}{2f_{\text{Geo}}} - k \frac{x^2 + y^2}{2f_{\text{Pro}}} \quad (2)$$

Here,  $\sigma_{R,L} = +1$  or  $-1$  indicates the RCP or LCP component, respectively. The symbol  $k = 2\pi/\lambda$  represents the wave vector, where  $\lambda$  is the wavelength of operation. In addition,  $f_{\text{Geo}}$  and  $f_{\text{Pro}}$  denote the specified focal lengths of geometric and propagation phases, respectively. The term  $\Phi_{\text{Geo}}$  signifies that the nano-structured layer initially converges on the LCP and diverges

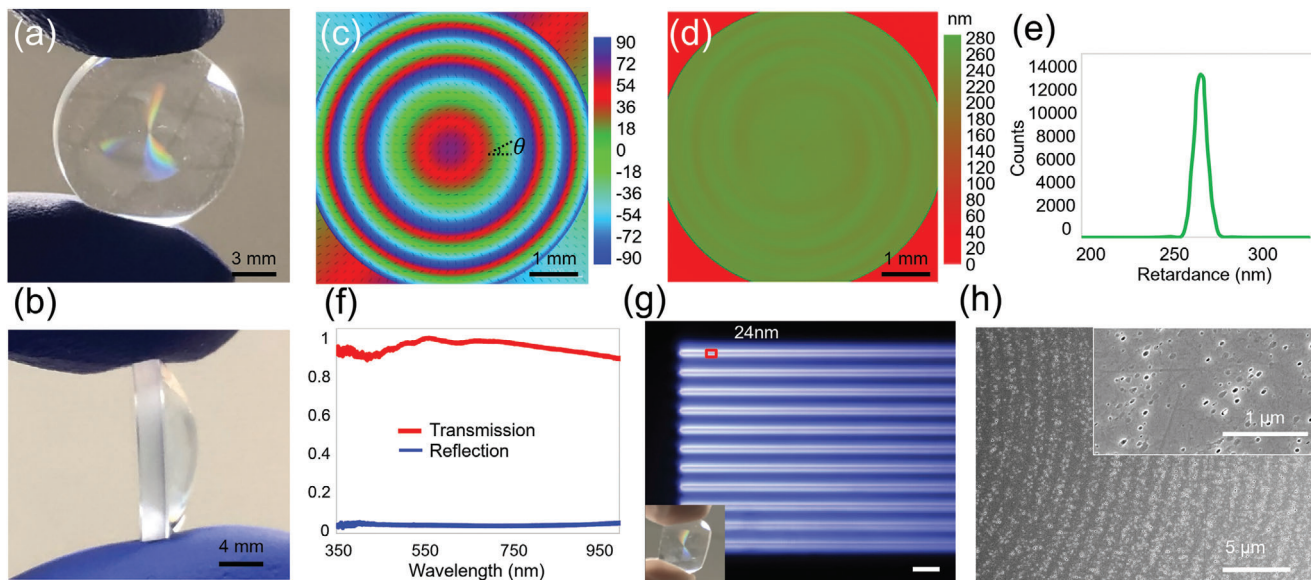


**Figure 2.** Characterization of the fabricated sample. a) Top-view photograph of the meta-device sample. b) Side-view photograph of the meta-device sample. c) Orientation angle of the optical axis. d) Measurement of the phase retardance distribution for the meta-device samples. e) Retardance distribution. f) Wavelength dependent transmission and reflection spectrum of the fabricated sample. g) Dark-field image of the cross-section of the fabricated sample. Scale bar: 50  $\mu\text{m}$ . h) Scanning electron microscope (SEM) image of the fabricated sample.

on the RCP component. On the other hand,  $\Phi_{\text{Pro}}$ , signifying the propagation phase, is employed to slightly increase the focal length of LCP and invert the RCP, causing it to converge instead of diverging and attain a comparable focal distance with LCP, as illustrated in Figure 1c. By carefully designing  $f_{\text{Geo}}$  (4.6 m) and  $f_{\text{Pro}}$  (20.1 mm), the focal lengths of LCP and RCP can be determined as 20.2 and 20 mm, respectively, based on the equation  $f_{\text{R,L}} = \frac{f_{\text{Pro}}f_{\text{Geo}}}{f_{\text{Geo}} \pm f_{\text{Pro}}}$ . For the parameter design and the simulated results of the meta-devices, see Sections S4 and S5, Supporting Information. As depicted in Figure 1d, when the image system is illuminated by linearly polarized light, it becomes possible to capture both underfocused and overfocused images by positioning the detection plane in the middle of the two imaging planes corresponding to the two circular polarizations. In addition, to adhere to the preference for a single shot approach, strategically placing a polarized camera between the two focal positions facilitates the acquisition of images under both underfocused and overfocused conditions. This configuration enables the measurement of the object's phase distribution through the acquisition of intensity variation along the propagation direction by solving the TIE equation.<sup>[10]</sup> Further discussion will be provided in the subsequent Experimental Section.

For the proof of concept, a meta-device, covering a 6 mm-diameter pattern area, is created through birefringence patterning using laser writing technology on a fused silica plano-convex lens substrate with a 1/2 inch diameter, as depicted in Figure 2a,b. Figure 2c–h primarily focuses on the characterization of the fabricated sample. Figure 2c illustrates the local optical axis distribution  $\theta$  of the fabricated metasurface. The phase distribution of the designed meta-device is twice the orientation angle,  $\theta$ . In Figure 2d,e, the phase retardance value and uniformity of the fabricated sample are displayed, indicating that the meta-device achieves a 264 nm phase retardance for a working wave-

length of 528 nm to attain half-wavelength retardance. The measured transmission of the manufactured meta-device is  $\approx 95\%$  at the designed working wavelength and a low reflection, as demonstrated in Figure 2f. To characterize the fabricated sample from a side view, we polish the sample substrate with a rough grid until the sample structure is exposed to the air, as depicted in Figure 2g. For the polishing procedure of the meta-device, refer to Section S12, Supporting Information. Figure 2h presents the measured scanning electron microscope (SEM) imaging of the fabricated sample.

The working mechanism of the laser writing technology can be elucidated as follows: when focused fs laser pulses irradiate silica glass, laser-induced cavitation in the glass gives rise to numerous nanopores with dimensions in the tens of nm. Subsequently, the near-field enhancement effect reshapes these nanopores into oblate forms, oriented perpendicular to the polarization direction of the writing laser beam.<sup>[33]</sup> The modification induced by nanopores exhibits form birefringence, a property that can be finely tuned by adjusting laser writing parameters such as pulse energy and density for retardance, and polarization direction for the orientation of the slow axis. This adaptability makes nanopores-based modifications suitable for fabricating high-efficiency meta-devices with desired retardance and slow-axis azimuth distribution.<sup>[34]</sup> See Section S6, Supporting Information for more details.

It is crucial to note that the employed working principle is conceptually akin to the transport intensity equation. Two images are used in the computation of the quantitative phase image, incorporating various artificial objects. Figure 3 illustrates the resultant QPI for artificial objects made by  $\text{SiO}_2$ . The objects are fabricated using a mask-less photolithography process with thicknesses variations of 80, 140, 200, and 240 nm. The detailed

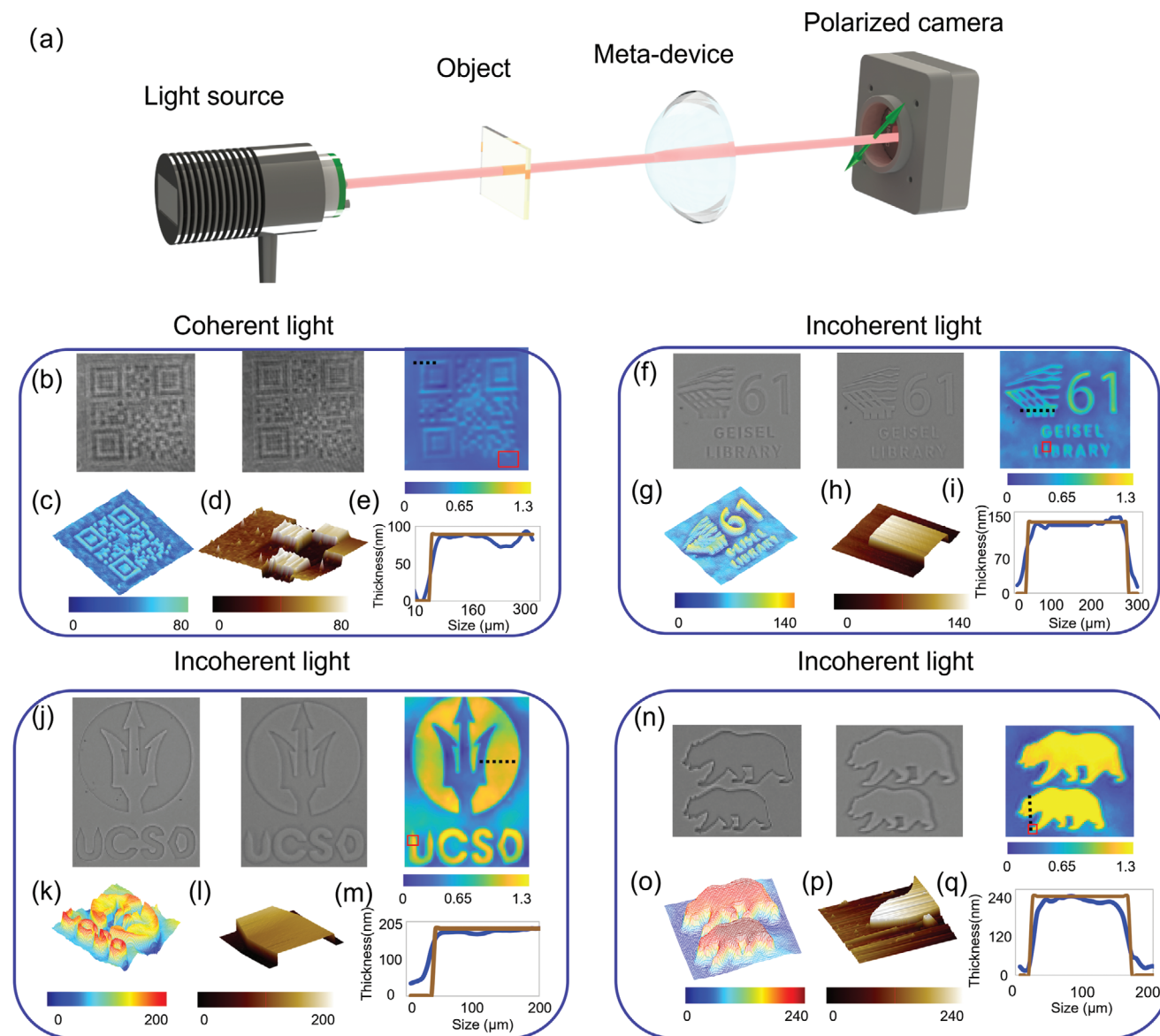


**Figure 3.** Free space experiment. a) Experimental setup for the artificial phase object. b) Overfocused and underfocused images, along with the extracted QPI (the red frame indicates the measured AFM areas), is obtained for an 80 nm QR code object for Zhaowei Liu's research group, captured by a polarized camera. c) The perspective view of the QPI images; the color bar indicates the thickness of the object (unit: nm). d) The thickness profile from the AFM measurement. e) A comparison between QPI and AFM results along the dashed line in the right panel of (b). f–i), j–m), and n–q) The samples with different thicknesses: 140, 200, 240 nm.

fabrication process is outlined in the Experimental Section. The experimental setup is presented in Figure 3a, where linearly polarized light passes through the meta device, causing the separation of LCP and RCP light along the propagation direction due to different focal lengths. A quarter wave plate placed in the front of the polarized camera is employed for the preparation of image subtraction in the TIE algorithm.<sup>[35]</sup> For further details, refer to Section S1, Supporting Information. Here, we denote the distance from the object to the meta-device as  $d_1$  and the distance from the metalens to the polarization camera as  $d_2$ . The relationship is defined by  $\frac{1}{d_1} + \frac{1}{d_2} = \frac{1}{f_{\text{PTO}}}$ . It is noteworthy that, for the ex-

periment, we aim to demonstrate that our design not only works for incoherent light but also for coherent light. In Figure 3b–e, featuring the QR code object for Zhaowei Liu's research group, the illuminated light source is a supercontinuum laser (SuperK EXW-12, NKT Photonics). Under laser illumination, both under-focused  $I(x, y, -dz)$  and overfocused  $I(x, y, +dz)$  images are captured in the left two panels of Figure 3b. Subsequently, we calculate the intensity variation distribution  $\Delta I = I(x, y, +dz) - I(x, y, -dz)$  for  $\Delta z = 200 \mu\text{m}$  (the focal distance difference between the LCP and RCP components), which is essential for our phase reconstruction. This reconstruction employs a universal solver to

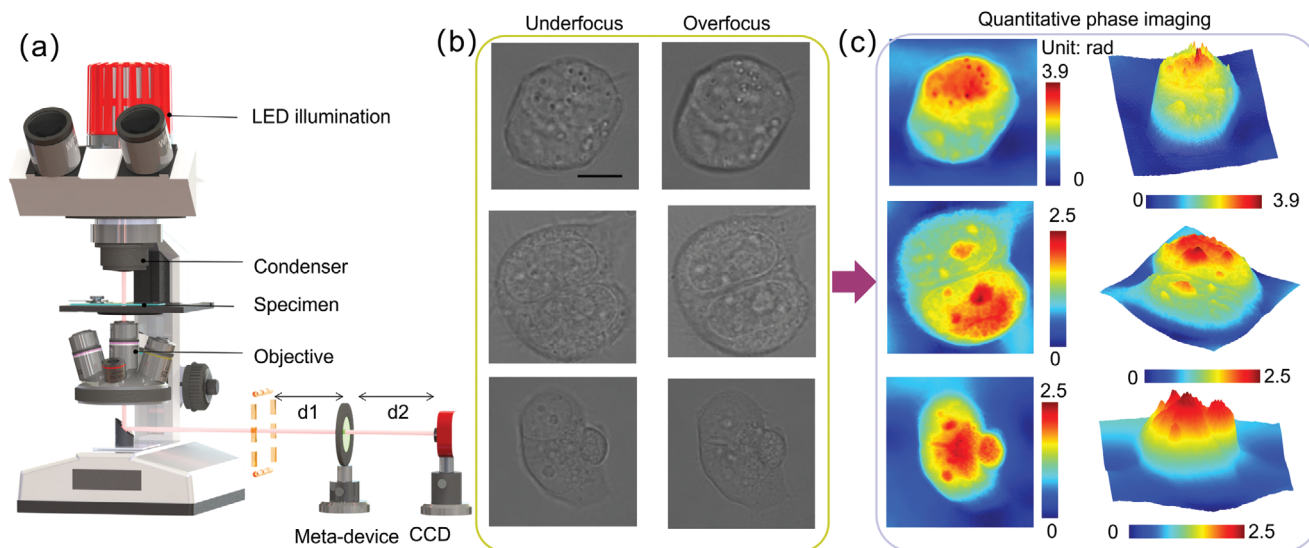


**Figure 4.** a) Optical setup. The meta-device relays the image from the image plane of the microscope, that is, the brown dash frame, to the imaging CCD by satisfying the condition  $\frac{1}{d_1} + \frac{1}{d_2} = \frac{1}{f_{pro}}$ . b) Underfocussed and overfocussed images of different cell morphological. The scale bar is  $2.5 \mu\text{m}$ . c) The QPI imaging results of HEK cells with different stages.

calculate the equation  $-k \frac{\partial I(x,y)}{\partial z} = \nabla_{\perp} [I(x,y) \nabla_{\perp} \Psi(x,y)]$ , where  $\nabla_{\perp}$  is transverse gradient operator.<sup>[35]</sup> The detailed reconstruction algorithm is provided in Section S7, Supporting Information. The right panel of Figure 3b depicts the experimentally reconstructed phase profile  $\Psi(x,y)$  of the object. The captured intensity images exhibit discernable speckles; although, the extracted phase is not significantly affected. However, for most applications, incoherent light will be more favorable as it reduces speckles with a uniform illumination naturally. Therefore, in Figure 3f,j,n, we use an incoherent light source, specifically an LED light (Thorlabs, M530L4-C1) coupled with a spectral filter ( $528 \text{ nm} \pm 1.4$ , Edmund Optics). The resulting image appears more uniform and exhibits fewer speckles. For a better comparison, we also conduct experiments with the same sample under both incoherent and coherent light illumination (Section S8, Supporting Information). As the phase shift  $\Psi$  is directly proportional to the optical thickness, the thickness can be estimated from the phase  $\Psi$ , considering the refractive index of silica and the operational wavelength:  $t_{\text{SiO}_2} = \frac{\lambda \times \Psi}{2\pi(n_{\text{SiO}_2} - n_{\text{air}})}$ . Here  $n$  is the refractive index,  $n_{\text{SiO}_2} = 1.4609$ ,  $n_{\text{air}}$  is 1, and  $\lambda = 528 \text{ nm}$  is the working wavelength. The extracted thickness distribution of the objects is shown in Figure 3c,g,k,o. Specifically, Figure 3d,h,l,p depicts the thickness measurements acquired through atomic force microscopy (AFM); while, Figure 3e,i,m,q presents a comparative analysis between QPI and AFM measurements. The observed agreement between these measurements underscores the system's proficiency in retrieving quantitative phase data (Section S9, Supporting Information). For the results in Figure 3c,g,k,o, the outcomes reveal a noticeable increase in the phase value corresponding to the augmentation of structure thickness.

Our EIMPI technology holds significant promise in the field of life sciences as it facilitates the direct detection of thickness in live specimens within biological samples. The variability in thickness may provide essential information about cell health, biolog-

ical function, and response to environmental stimuli, with potential implications for understanding cell behavior and disease mechanisms.<sup>[36]</sup> Our proposed EIMPI is completely compatible with a standard commercial microscope setup as it operates with incoherent light, eliminating the need to alter the illumination. In Figure 4a, our meta-device is positioned at the image plane of Zeiss inverted microscope (Carl Zeiss Microscopy, Munich, Germany), with an objective 1.2 NA, 60 $\times$ . As depicted in the top panel of Figure 4b, the cells exhibit various stages, representing normal growth and metabolic activities. The middle panel illustrates nucleus and cell division, resulting in two identical daughter cells. The process of cell division leads to the formation of two genetically identical daughter cells. The bottom panel shows the physical separation of one cell. By capturing the underfocussed and overfocussed images, the reconstructed QPI images of top view and perspective view can be obtained, as shown in Figure 4c. Note that the image resolution of the cells is crucial for the biological field. In this work, the obtained image resolution is  $\approx 230 \text{ nm}$ ; which is close to the diffraction limit  $220 \text{ nm} (\lambda/2\text{NA})$ . For more details, see Section S10, Supporting Information.

Laser ablation, also known as “laser microsurgery,” alters cellular and intracellular structures at a microscopic level. It has been increasingly utilized to explore metabolic variations within cell populations through in situ analysis of individual cells based on the mass spectrum analysis.<sup>[37]</sup> In this context, we propose another visualization method with quantitative information about the single cell ablation. An 80 MHz Ti:Sapphire laser, operating at an 800 nm wavelength and generating an  $\approx 100 \text{ fs}$  beam, facilitates the process. The light is directed to the Zeiss inverted microscope's port through highly reflective coated mirrors. A single dual-axis fast scanning mirror (FSM-300-01, Newport) enables precise scanning within the microscope optical field using a 60 $\times$  (1.2 NA) microscope objective. Pulse energy at the focused spot is modulated by adjusting the orientation of a Glan-Thompson polarizer on a motorized rotational stage. LabVIEW is utilized for

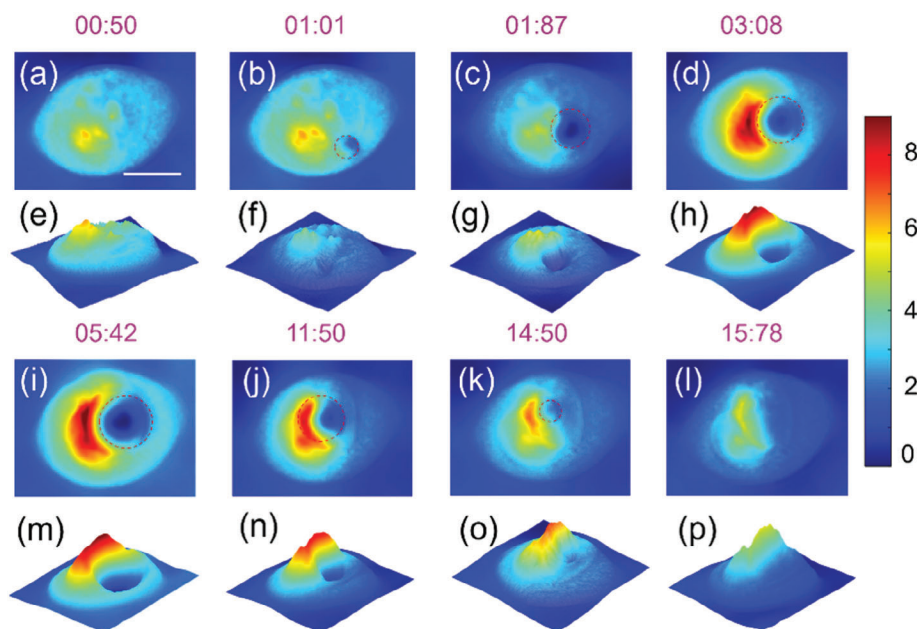


**Figure 5.** EIMPI enables time-lapse of a HEK cell culture undergoing laser ablation. The title number: before the colon, the unit is in seconds (s); after the colon, the unit is in milliseconds (ms). a–d) and i–l) These panels present the QPI results at different times, as indicated. e–h) and m–p) These panels display the corresponding stereoscopic view images. Scale bar: 5  $\mu\text{m}$ . The red dash circular indicates the laser position.

communication and control of the polarized camera controller, as well as for scanning mirror control. This setup enables the creation of patterns with any desired geometry in the target cell or organelle. In **Figure 5**, a red circular dash line indicates the trajectory of the line used to cut the cell from the bottom right to top left. Utilizing our EIMPI scheme, we obtain the final quantitative microscopic imaging over time. This experiment demonstrates the efficacy of quantitative microscopic imaging in laser-induced ablation in HEK cells. Residues remain in the vicinity of the cutting section, as shown in **Figure 5l**. The relationship between laser ablation and QPI lies in their combined application in studying dynamic cellular processes. When combined with laser ablation, this imaging method can provide real-time visualization of laser-induced cellular changes, offering comprehensive insights into the direct and subsequent impacts on cell morphology and function.

### 3. Discussion

We would like to highlight several advantages of the proposed EIMPI scheme. First, in comparison to interference based on the phase-shifting method for extracting phase gradient information, our method directly obtains the phase information. This eliminates the necessity for integration along the  $x$  and  $y$  directions, thereby avoiding the accumulation of background noise. In addition, without non-common path-length interference, the system exhibits stability, which is user friendly. Second, our EIMPI system is more lightweight and compact, requiring no additional  $4f$  system preparation or imaging lenses. Third, our method does not require modifications to the illumination, allowing for the direct extraction of phase information and compatibility with traditional bright field microscopes. Fourth, EIMPI operates with an incoherent light source, resulting in speckle-free imaging and

demonstrating suitability for strong light-sensitive biomedical specimens. Fifth, its single-shot capability accelerates data acquisition, thereby enhancing efficiency in experimental settings. When employing a universal solver to calculate the TIE, the total computation time is 0.09 s on a 2.6 GHz laptop. We would also like to mention that it is feasible to design and fabricate a meta-lens of a relatively large size capable of generating different focal lengths for LCP and RCP components to achieve the same experimental results, instead of using the plano-convex lens, which will make the whole system more compact.

In summary, we propose and demonstrate Eagle-Eye-Inspired Phase Imaging (EIMPI), a scheme in QPI tailored for dynamic observation of unlabeled specimens. Our method relies solely on the combination of geometric and propagation phase elements in an integrated meta-device, separating LCP and RCP image planes along the propagation axis. By placing a polarized camera between the two focal planes, quantitative phase information is obtained based on intensity deviation using TIE. We demonstrate its application in free-space experiments, requiring only the assistance of QPW. The working scheme is also applied to cells, calculating their thickness information. Additionally, we observe that EIMPI can be used for laser ablation, engaging in dynamic specimen observations without the need for labeling to provide quantitative information. The proposed EIMPI, characterized by its simple and compact design, holds promise for significant applications in fields such as microscopy and endoscopy.

### 4. Experimental Section

**Metasurface Fabrication:** The entire process was executed using an ultrafast laser operating at a wavelength of 1030 nm, with a pulse duration of 300 fs. The incident laser was focused by a numerical aperture of 0.16, and its polarization was controlled by a half-wave plate. Consequently,

manipulation of the distribution of slow axis birefringence was achieved by altering the polarization azimuth of the writing beam using a half-wave plate. The meta-device was fabricated 50  $\mu\text{m}$  away from the flat surface of the plano-convex lens. Scanning along the designated path could be repeated at different depths within the sample thickness by adjusting the position of the sample relative to the focusing arrangement along the beam propagation direction. This allowed for the fabrication of more than one layer of nanostructures onto the metasurface to obtain the desired phase retardance. The single-layered sample of this study was also fabricated for reference. Please refer to Section S6, Supporting Information.

**Phase Object Preparation:** The artificial phase mask was fabricated using a mask-less photolithography process. This comprehensive fabrication procedure was performed in part at the San Diego Nanotechnology Infrastructure (SDNI) of UCSD, a member of the National Nanotechnology Coordinated Infrastructure (NNCI), which was supported by the National Science Foundation (Grant ECCS-2025752). Initially, diced silicon dioxide ( $15 \times 15 \times 0.5 \text{ mm}^3$ , double face polishing) was subjected to sonication in acetone, isopropanol (IPA), and deionized (DI) water, followed by prebaking at 180  $^{\circ}\text{C}$  for 10 min. Subsequently, a negative photoresist (NR9-1500) was spin-coated onto the wafer at 3500 rpm for 40 s, forming a film  $\approx 1.5 \mu\text{m}$  thick. The soft bake process was then conducted at 150  $^{\circ}\text{C}$  for 3 min on a hotplate. Following this, the designed pattern creation was executed using AutoCAD, a computer-aided design software. Subsequently, a mask-less photolithography machine (Heidelberg MLA150) was employed for UV exposure (laser wavelength: 375 nm, dose: 1350  $\text{mJ cm}^{-2}$ ), followed by a post-exposure bake process at 100  $^{\circ}\text{C}$  on the hotplate for 3 min. The wafer was then immersed in RD6 developer for 12 s with agitation and rinsed with DI water for 3 min. A nitrogen gun was employed to evaporate any residual solvent. Following development, dry etching was conducted in the Oxford Plasmalab 80 Plus reactive ion etching (RIE) machine, employing CHF<sub>3</sub> gas for chemical etching (with an etching rate of 60  $\text{nm min}^{-1}$ ) and utilizing argon for protection. Subsequently, an etch-back process was executed by immersing the sample in Remover RR41 and rinsing it with acetone. By varying the etching time, samples with different thicknesses were obtained.

**Cell Preparation:** HEK 293 cells were grown on 60 mm Nunc cell culture dishes (ThermoFisher) and bathed in growth medium consisting of Advanced Dulbecco's modified Eagle medium supplemented with 10% heat inactivated fetal bovine serum and 1 $\times$  Glutamax (Gibco, ThermoFisher). The cells were maintained in a humidified incubator set to a temperature of 37  $^{\circ}\text{C}$  and 5% CO<sub>2</sub>. One to two days prior to experiments, cells were washed three times with Hanks Buffered Saline Solution (HBSS; ThermoFisher) devoid of calcium. They were then gently detached with 1 mL of 1 $\times$  TrypLE Express Enzyme (Gibco, ThermoFisher). Cells were viewed after 5 min in TrypLE to check for detachment. If detachment was not observed, they were incubated in TrypLE an additional 5 min. Upon detachment, TrypLE was quenched by the addition of 4 mL of growth medium. Detached cells were then seeded onto 35 mm glass bottom imaging dishes (Cell E. & G.) with growth medium at a cell density of 5–10% to facilitate single cell imaging. The volume in the 35 mm dishes was brought up to 2 mLs with growth medium. Cells were imaged on a heated stage incubator in the growth medium described above to maintain optimal health conditions.

## Supporting Information

Supporting Information is available from the Wiley Online Library or from the author.

## Acknowledgements

The authors wish to acknowledge fruitful conversations with Yuhao Lei as well as with Yunhui Gao. The generous partial support of this work by the Gordon and Betty Moore Foundation (to Z.L.) is also acknowledged.

## Conflict of Interest

The authors declare no conflict of interest.

## Author Contributions

J.Z. and Z.L. proposed the idea. J.Z. built the experimental setup and did the measurements. J.Z. did the simulation part and designed the meta-device sample. F.T. fabricated the artificial object and J.H. did the AFM measurement. J.Z. conducted the meta-device characterization. Z.S. and V.G.G. grew the cell samples. J.Z. prepared all the figures. All the authors discussed the results and prepared the paper. Z.L. supervised this work. All authors revised the manuscript.

## Data Availability Statement

The data that support the findings of this study are available in the supplementary material of this article.

## Keywords

meta-devices, metalens, quantitative phase imaging

Received: February 22, 2024

Revised: May 14, 2024

Published online: June 6, 2024

- [1] G. Byrne, D. Dimitrov, L. Monostori, R. Teti, F. Van Houten, R. Wertheim, *CIRP J. Manuf. Sci. Technol.* **2018**, 21, 1.
- [2] F. Zernike, *Science* **1955**, 121, 345.
- [3] W. Lang, *Nomarski Differential Interference-Contrast Microscopy*, Carl Zeiss, Oberkochen **1982**.
- [4] G. Popescu, *Quantitative Phase Imaging Of Cells And Tissues*, McGraw-Hill Professional, New York, NY **2011**.
- [5] J. Park, B. Bai, D. Ryu, T. Liu, C. Lee, Y. Luo, M. J. Lee, L. Huang, J. Shin, Y. Zhang, D. Ryu, Y. Li, G. Kim, H.-S. Min, A. Ozcan, Y. Park, *Nat. Methods* **2023**, 20, 1645.
- [6] J. B. Weitzman, *J. Biol.* **2003**, 2, 3.
- [7] B. R. Kemper, D. Carl, J. R. Schnekenburger, I. Bredebusch, M. Schafer, W. Domschke, G. Von Bally, *J. Biomed. Opt.* **2006**, 11, 034005.
- [8] L. Tian, L. Waller, *Opt. Express* **2015**, 23, 11394.
- [9] G. Zheng, R. Horstmeyer, C. Yang, *Nat. Photonics* **2013**, 7, 739.
- [10] M. R. Teague, *J. Opt. Soc. Am.* **1983**, 73, 1434.
- [11] Y. Gao, L. Cao, *Light Adv. Manuf.* **2023**, 4, 6.
- [12] N. Yu, P. Genevet, M. A. Kats, F. Aieta, J.-P. Tetienne, F. Capasso, Z. Gaburro, *Science* **2011**, 334, 333.
- [13] D. Lin, P. Fan, E. Hasman, M. L. Brongersma, *Science* **2014**, 345, 298.
- [14] J. Zhou, S. Liu, H. Qian, Y. Li, H. Luo, S. Wen, Z. Zhou, G. Guo, B. Shi, Z. Liu, *Sci. Adv.* **2020**, 6, eabc4385.
- [15] J. Zhou, H. Qian, C.-F. Chen, J. Zhao, G. Li, Q. Wu, H. Luo, S. Wen, Z. Liu, *Proc. Natl. Acad. Sci. U. S. A.* **2019**, 116, 11137.
- [16] J. Zhou, J. Zhao, Q. Wu, C.-F. Chen, M. Lei, G. Chen, F. Tian, Z. Liu, *Adv. Funct. Mater.* **2022**, 32, 2204734.
- [17] G. Kim, Y. Kim, J. Yun, S.-W. Moon, S. Kim, J. Kim, J. Park, T. Badloe, I. Kim, J. Rho, *Nat. Commun.* **2022**, 13, 5920.
- [18] D. Jeon, K. Shin, S.-W. Moon, J. Rho, *Nano Converg.* **2023**, 10, 24.
- [19] L. Li, Z. Liu, X. Ren, S. Wang, V.-C. Su, M.-K. Chen, C. H. Chu, H. Y. Kuo, B. Liu, W. Zang, G. Guo, L. Zhang, Z. Wang, S. Zhu, D. P. Tsai, *Science* **2020**, 368, 1487.
- [20] L. Deng, Y. Xu, R. Jin, Z. Cai, Y. Liu, *Adv. Opt. Mater.* **2022**, 10, 2200910.
- [21] J. Zhang, P. Li, R. C. Cheung, A. M. Wong, J. Li, *Adv. Photonics* **2023**, 5, 036001.
- [22] G. Zheng, H. Mühlenbernd, M. Kenney, G. Li, T. Zentgraf, S. Zhang, *Nat. Nanotechnol.* **2015**, 10, 308.
- [23] H. He, Y. Zhang, Y. Shao, Y. Zhang, G. Geng, J. Li, X. Li, Y. Wang, L. Bian, J. Zhang, L. Huang, *Adv. Mater.* **2024**, 2313357.

- [24] J. Zhou, Q. Wu, J. Zhao, C. Posner, M. Lei, G. Chen, J. Zhang, Z. Liu, *Phys. Rev. Lett.* **2022**, 129, 020801.
- [25] Q. Wu, J. Zhou, X. Chen, J. Zhao, M. Lei, G. Chen, Y.-H. Lo, Z. Liu, *Optica* **2023**, 10, 619.
- [26] E. Engay, D. Huo, R. Malureanu, A.-I. Bunea, A. Lavrinenko, *Nano Lett.* **2021**, 21, 3820.
- [27] H. Kwon, E. Arbabi, S. M. Kamali, M. Faraji-Dana, A. Faraon, *Nat. Photonics* **2020**, 14, 109.
- [28] Y. Liang, K. Koshelev, F. Zhang, H. Lin, S. Lin, J. Wu, B. Jia, Y. Kivshar, *Nano Lett.* **2020**, 20, 6351.
- [29] H. Zhou, X. Li, N. Ullah, G. Geng, J. Li, X. Li, Y. Wang, L. Huang, *Appl. Phys. Lett.* **2022**, 120, 161702.
- [30] M. V. Berry, *Proc. R. Soc. London, Ser. A* **1984**, 392, 45.
- [31] S. Pancharatnam, *Proc. - Indian Acad. Sci., Sect. A* **1956**, 44, 398.
- [32] A. Sedgley, A. Ahearn, The Eagle Eye, **2023**, <https://www.birdnote.org/listen/shows/eagle-eye>.
- [33] M. Sakakura, Y. Lei, L. Wang, Y.-H. Yu, P. G. Kazansky, *Light: Sci. Appl.* **2020**, 9, 15.
- [34] Y. Lei, G. Shayeganrad, H. Wang, M. Sakakura, Y. Yu, L. Wang, D. Kliukin, L. Skuja, Y. Svirko, P. G. Kazansky, *Light: Sci. Appl.* **2023**, 12, 74.
- [35] J. Zhang, Q. Chen, J. Sun, L. Tian, C. Zuo, *Opt. Lett.* **2020**, 45, 3649.
- [36] I. A. Hatton, E. D. Galbraith, N. S. C. Merleau, T. P. Miettinen, B. M. Smith, J. A. Shander, *Proc. Natl. Acad. Sci. U. S. A.* **2023**, 120, 2303077120.
- [37] B. Shrestha, A. Vertes, *Anal. Chem.* **2009**, 81, 8265.